



Cite this: *Phys. Chem. Chem. Phys.*,  
2015, 17, 32033

# Improving the electrochemical properties of $\text{LiNi}_{0.5}\text{Co}_{0.2}\text{Mn}_{0.3}\text{O}_2$ at 4.6 V cutoff potential by surface coating with $\text{Li}_2\text{TiO}_3$ for lithium-ion batteries

Jing Wang,<sup>a</sup> Yangyang Yu,<sup>a</sup> Bing Li,<sup>b</sup> Tao Fu,<sup>a</sup> Dongquan Xie,<sup>a</sup> Jijun Cai<sup>a</sup> and Jinbao Zhao<sup>\*ab</sup>

The  $\text{Li}_2\text{TiO}_3$ -coated  $\text{LiNi}_{0.5}\text{Co}_{0.2}\text{Mn}_{0.3}\text{O}_2$  (LTO@NCM) cathode materials are synthesized *via* an *in situ* co-precipitation method followed by the lithiation process and thermal annealing. The  $\text{Li}_2\text{TiO}_3$  coating layer is designed to strongly adhere to the core-material with 3D diffusion pathways for  $\text{Li}^+$  ions. Electrochemical tests suggest that compared with pristine NCM,  $\text{Li}_2\text{TiO}_3$  serves as both a Li ion conductive layer and a protective coating layer against the attack of HF in the electrolyte, and remarkably improves the cycling performance at higher charged state and rate capability of the LTO@NCM composite material. What is more, phase transformation of NCM and dissolution of metal ions at high-temperatures at 4.6 V cutoff potential are effectively suppressed after LTO-coating. Our study demonstrates that LTO-coating on the surface of NCM is a viable method to improve the electrochemical performance of NCM, especially at high rates and under high-voltage charged conditions.

Received 6th September 2015,  
Accepted 4th November 2015

DOI: 10.1039/c5cp05319f

www.rsc.org/pccp

## Introduction

High performance rechargeable batteries are required to fulfill the rapidly growing demand for electric (EV), hybrid electric (HEV) and plug-in hybrid electric vehicles (PHEV).<sup>1–6</sup> Due to high voltage, high specific capacity, excellent cycling life and other advantages, lithium ion batteries (LIBs) are regarded as the most likely power source for electrical vehicles rather than the ‘old-type’ rechargeable batteries.<sup>7,8</sup> Substantial research studies have proved that the performance of lithium-ion batteries was mainly determined by the property of the cathode materials and thus great efforts have been made to optimize the cathode materials with high energy density.<sup>9</sup>

The primary approach to improve the energy density of batteries is to develop cathode materials with high capacity<sup>10</sup> or/and higher operating voltages.<sup>11</sup> In this respect, layered nickel-rich oxide  $\text{LiNi}_{0.5}\text{Co}_{0.2}\text{Mn}_{0.3}\text{O}_2$  is a competitive candidate owing to its low cost, low toxicity and high specific capacity compared with the mainstream commercial  $\text{LiCoO}_2$ .<sup>12,13</sup> However, poor cycling performance and inferior thermal stability of  $\text{LiNi}_{0.5}\text{Co}_{0.2}\text{Mn}_{0.3}\text{O}_2$ , especially at high operating voltages

(~4.6 V) and high temperatures (~55 °C), have hindered its widespread application.<sup>14</sup> The chief reason lies in the chemistry that the unstable  $\text{Ni}^{4+}$  ion in the delithiated  $\text{Li}_{1-\delta}[\text{Ni}_{1-x}\text{M}_x]\text{O}_2$  materials is readily reduced to  $\text{Ni}^{3+}$ , which causes a structural transformation to form a more stable rock salt phase ( $\text{Li}_x\text{Ni}_{1-x}\text{O}$ , NaCl structure) and a spinel  $\text{Li}(\text{Ni}_{0.5}\text{Co}_{0.2}\text{Mn}_{0.3})_2\text{O}_4$  phase,<sup>15</sup> resulting in an increase in the interfacial impedance and the cycling instability of the cell.<sup>16,17</sup> Meanwhile, the structure of the delithiated Ni-rich material becomes thermally unstable due to oxygen release from the structure, and upon contact with an organic electrolyte,<sup>18</sup> the highly-active delithiated  $\text{Li}_{1-\delta}[\text{Ni}_{1-x}\text{M}_x]\text{O}_2$  can oxidatively break down the electrolyte molecules and potentially cause a severe thermal runaway with flame and explosion, as a result of the interaction between the organic electrolyte and highly active delithiated  $\text{Li}_{1-\delta}[\text{Ni}_{1-x}\text{M}_x]\text{O}_2$ .<sup>19</sup>

A conventional method to improve the electrochemical stability and thermal properties of cathode materials for LIBs is surface modification (such as coating) of the materials with metal oxides, metal phosphates and so on. Various inorganic compounds, such as  $\text{LiAlO}_2$ ,<sup>20</sup>  $\text{LiTiO}_2$ ,<sup>21</sup>  $\text{Li}_2\text{ZrO}_3$ ,<sup>22</sup>  $\text{Al}(\text{OH})_3$ ,<sup>23</sup>  $\text{AlF}_3$ ,<sup>24</sup>  $\text{Ni}_3(\text{PO}_4)_2$ ,<sup>17</sup>  $\text{TiO}_2$ ,<sup>25</sup>  $\text{Bi}_2\text{O}_3$ <sup>26</sup> and  $\text{FePO}_4$ ,<sup>27</sup> have been investigated as surface coating agents (usually a thin layer) to improve the cycling performance and thermal stability of cathode materials. The coating layers improve the interface stability between the active material and the electrolyte, protecting the active cathode materials from the attack of HF generated in the electrolyte during cycling and suppressing further the oxygen

<sup>a</sup> State Key Lab of Physical Chemistry of Solid Surfaces, Department of Chemistry, Collaborative Innovation Center of Chemistry for Energy Materials, College of Chemistry and Chemical Engineering, Xiamen University, Xiamen, 361005, P. R. China. E-mail: jbzha@xmu.edu.cn

<sup>b</sup> School of Energy Research, Xiamen University, Xiamen, 361005, P. R. China

loss from the material.<sup>16,28</sup> As a result, the structural integrity, the electrochemical properties especially at high-temperatures, and the thermal stability at the highly delithiated state of Ni-rich  $\text{Li}[\text{Ni}_{1-x}\text{M}_x]\text{O}_2$  cathode materials can be much improved.

Lithium ion conductive  $\text{Li}_2\text{TiO}_3$  is electrochemically inert in a wide voltage range and structurally stable in the organic electrolyte.<sup>29</sup> This inert coating layer can prevent the direct contact between the highly active delithiated  $\text{Li}_{1-\delta}[\text{Ni}_{1-x}\text{M}_x]\text{O}_2$  and the electrolyte,<sup>28</sup> so the electrolyte decomposition by  $\text{Ni}^{4+}$  and  $\text{Co}^{4+}$  oxidation is expected to be relieved and the cathode structure corrosion by HF in the electrolyte is expected to be relieved as well.<sup>30</sup> Furthermore, the  $\text{Li}^+$  diffusion path is three-dimensional in  $\text{Li}_2\text{TiO}_3$  and its ionic conductivity could be increased when doped with aliovalent ions as a result of vacancy formation.<sup>28</sup> In this regard, it is possible that a doped  $\text{Li}_2\text{TiO}_3$  coating layer is helpful to improve the rate capability as well as the cycling stability of  $\text{Li}[\text{Ni}_{1-x}\text{M}_x]\text{O}_2$  materials.

In this work, lithium ion conductive  $\text{Li}_2\text{TiO}_3$  has been used to coat the surface of Ni-rich  $\text{LiNi}_{0.5}\text{Co}_{0.2}\text{Mn}_{0.3}\text{O}_2$  cathode materials for LIBs. The  $\text{Li}_2\text{TiO}_3$ -modified  $\text{LiNi}_{0.5}\text{Co}_{0.2}\text{Mn}_{0.3}\text{O}_2$  samples were prepared by a two-step reaction that involves an *in situ* hydrolysis of  $\text{Ti}(\text{SO}_4)_2$  on the surface of the  $\text{LiNi}_{0.5}\text{Co}_{0.2}\text{Mn}_{0.3}\text{O}_2$  precursor ( $[\text{Ni}_{0.5}\text{Co}_{0.2}\text{Mn}_{0.3}](\text{OH})_2$ ), which could obtain a uniform  $\text{Li}_2\text{TiO}_3$ -precursor ( $\text{TiO}_2$ ) coating, and a subsequent lithiation process with LiOH. In the lithiation process, some Ti may enter into the host  $\text{LiNi}_{0.5}\text{Co}_{0.2}\text{Mn}_{0.3}\text{O}_2$  cathode and a trace amount of M (M = Ni, Co, Mn) could also enter into the  $\text{Li}_2\text{TiO}_3$  phase to form the doped material. The composite materials present excellent cycling stability as well as improved thermal stability, especially at high cut-off voltages and high temperatures. Furthermore, the internal mechanism of the LTO effect on NCM is firstly tentatively explored.

## Experimental section

### Material preparation

The spherical precursor compound  $[\text{Ni}_{0.5}\text{Co}_{0.2}\text{Mn}_{0.3}](\text{OH})_2$  was purchased from Ningbo Jinhe New Materials Co., Ltd. After air-drying, 9.16 g of  $[\text{Ni}_{0.5}\text{Co}_{0.2}\text{Mn}_{0.3}](\text{OH})_2$  powder was put into an oven with 150 ml of deionized water and mixed under constant stirring at 55 °C. The calculated  $\text{Ti}(\text{SO}_4)_2$  and NaOH (1 : 4, n/n) were dissolved in deionized water separately, then the obtained solutions were subsequently injected into the above suspension dropwise. The  $[\text{Ni}_{0.5}\text{Co}_{0.2}\text{Mn}_{0.3}](\text{OH})_2$  samples coated with 1 wt%, 3 wt% and 5 wt%  $\text{TiO}_2$  were denoted 1%  $\text{TiO}_2@\text{NCMOH}$ , 3%  $\text{TiO}_2@\text{NCMOH}$  and 5%  $\text{TiO}_2@\text{NCMOH}$ , respectively. After filtration, the precursor was washed with distilled water and alcohol several times. The dried precursor was mixed with an appropriate amount of LiOH, then ball-milled at 200 rpm for 1 h (FRITSCH-Pulverisette 14). The ball-milled mixture was first sintered in an air atmosphere at 850 °C for 12 h, then cooled down naturally to room temperature. The  $\text{LiNi}_{0.5}\text{Co}_{0.2}\text{Mn}_{0.3}\text{O}_2$  samples coated with 1 wt%, 3 wt% and 5 wt%  $\text{Li}_2\text{TiO}_3$  were denoted 1% LTO@NCM, 3% LTO@NCM and 5% LTO@NCM, respectively.

### Material characterization

The XRD data were collected on a Rigaku miniflex 600 with Cu K $\alpha$  radiation operated at 40 kV and 15 mA scanned from 10° to 90° at 1° min<sup>-1</sup> with a step size of 0.02°. A field emission scanning electron microscope (SEM, HITACHI S-4800) was used to characterize the morphology of samples, and energy dispersive X-ray spectroscopy (EDS, OXFORD 7593-H, an accessory of SEM) was carried out to analyze the surface elemental distribution of particles with 20 kV acceleration voltage. Transmission electron microscopy (TEM, JEOL-2100) was used to examine the morphologies and identify the structures of the as-prepared samples. The X-ray photoelectron spectroscopy (XPS) data were collected using a Quantum 2000 Scanning ESCA Microprobe spectrometer with focused monochromatized Al K $\alpha$  radiation (1486.6 eV). The pass energies were 60 eV for the survey spectra and 20 eV for particular elements, respectively. The test samples are obtained from clipping the corresponding pasted electrode pole piece without sputtering processing. The DSC/TG (STA 449 F3 Jupiter Netzsch) was used to measure the thermal stability of electrodes from 100 °C to 400 °C at a heating rate of 5 °C min<sup>-1</sup> using an electrolyte of 1 M LiPF<sub>6</sub> salt dissolved in ethylene carbonate (EC) and dimethyl carbonate (DMC) with a mass ratio of 1 : 1 (#301 electrolyte, Guotai Huarong, China). The detailed measurements were as follows. Firstly, the button cell was cycled for one cycle and then charged to 4.6 V state. The charged cell was taken apart to get electrode material films in an Ar-filled glove box. The film was washed several times with DMC and dried naturally. The electrode materials scraped from the film and the electrolyte were sealed together in a gold-plated stainless steel crucible in the glove box. The ratio of electrolyte to electrode materials was 1  $\mu\text{L}$  of electrolyte per milligram of electrode materials.

### Electrochemical measurements

Electrochemical performances of these materials were evaluated with CR2016-type coin cell configuration. The working electrode film was obtained by spreading a slurry of 85 wt% active material, 8 wt% acetylene black, 2 wt% graphite black and 5 wt% polyvinylidene difluoride (PVDF) binder dispersed in *N*-methyl pyrrolidone (NMP) solvent onto an aluminum foil. After drying in a vacuum oven at 80 °C overnight, the electrode was punched out and roll-pressed. CR2016-type coin cells were assembled by sandwiching a porous polyethylene separator between the electrode and the Li metal foil in a high-purity Ar-filled glove box. The electrolyte was 1.0 M LiPF<sub>6</sub> salt dissolved in a solution of ethylene carbonate (EC) and dimethyl carbonate (DMC) with a weight ratio of 1 : 1. The mass loading for all the cells was controlled at about 5 mg cm<sup>-2</sup>.

The cells were charged with constant current and constant voltage mode (CC-CV), and discharged with specific constant current between 3.0 and 4.6 V at room temperature on battery testers (NEWARE BTS type battery charger, Shenzhen, China). Taking 1 C (170 mA g<sup>-1</sup>) as an example, the cells were first charged galvanostatically to 4.6 V, after 4.6 V was reached, the voltage was kept at 4.6 V until the current decreases gradually from 1 to 0.1 C (constant voltage charge step). The specific

capacity obtained was calculated basing on the composite material mass ( $\text{Li}_2\text{TiO}_3$  and  $\text{LiNi}_{0.5}\text{Co}_{0.2}\text{Mn}_{0.3}\text{O}_2$ ) in the electrode. Cyclic voltammogram (CV) measurements were performed on a CHI 660D potentiostat (Chenghua, Shanghai, China) at a scan rate of  $0.1 \text{ mV s}^{-1}$  with the potential range from 3.1 to 4.6 V. Electrochemical impedance spectra (EIS) were recorded using a Solartron SI 1287 workstation with a frequency range from 0.005 Hz to 100 kHz. All the tests were conducted at  $25^\circ\text{C}$  unless specified.

## Results and discussion

Fig. 1 shows the SEM images of precursor compounds:  $[\text{Ni}_{0.5}\text{Co}_{0.2}\text{Mn}_{0.3}](\text{OH})_2$  (a and b), 1%  $\text{TiO}_2@\text{NCMOH}$  (c and d), 3%  $\text{TiO}_2@\text{NCMOH}$  (e and f) and 5%  $\text{TiO}_2@\text{NCMOH}$  (g and h), respectively. The particles of the precursor  $[\text{Ni}_{0.5}\text{Co}_{0.2}\text{Mn}_{0.3}](\text{OH})_2$  are spherical with size ranging from  $6 \mu\text{m}$  to  $14 \mu\text{m}$ . Their surfaces as shown in Fig. 1b are smooth. After coating with  $\text{TiO}_2$ , the surfaces of  $\text{TiO}_2@\text{NCMOH}$  become rough with some small nanoparticles. At higher loading, for example, 5%  $\text{TiO}_2@\text{NCMOH}$  (Fig. 1h), the surface of  $[\text{Ni}_{0.5}\text{Co}_{0.2}\text{Mn}_{0.3}](\text{OH})_2$  is fully coated with a thick nanoparticle layer. EDS spectra of 3%  $\text{LTO}@\text{NCMOH}$  precursor were recorded to check the uniformity of the  $\text{TiO}_2$  coating layer on the surface of the coated

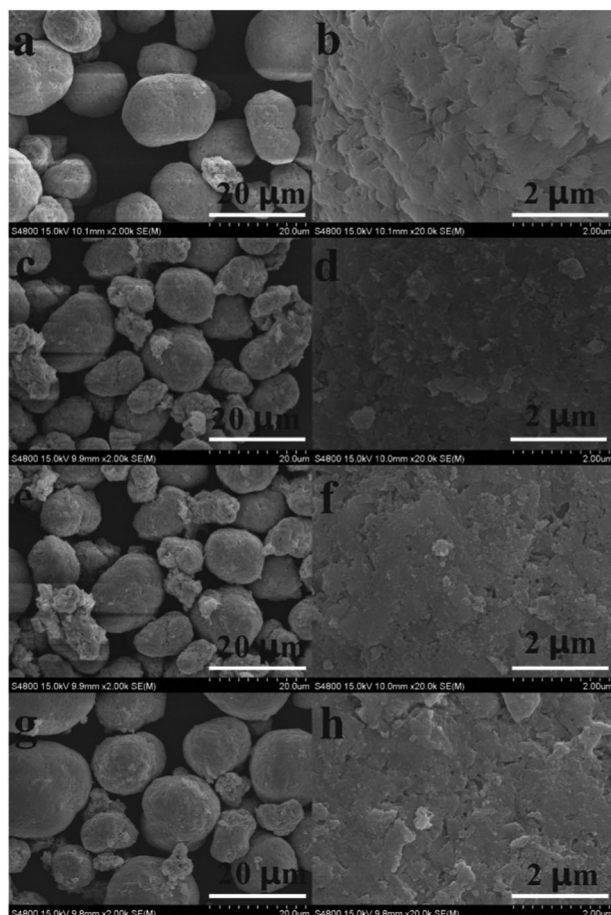


Fig. 1 SEM images of the precursor compound  $[\text{Ni}_{0.5}\text{Co}_{0.2}\text{Mn}_{0.3}](\text{OH})_2$  (a and b), 1%  $\text{TiO}_2@\text{NCMOH}$  (c and d), 3%  $\text{TiO}_2@\text{NCMOH}$  (e and f) and 5%  $\text{TiO}_2@\text{NCMOH}$  (g and h).

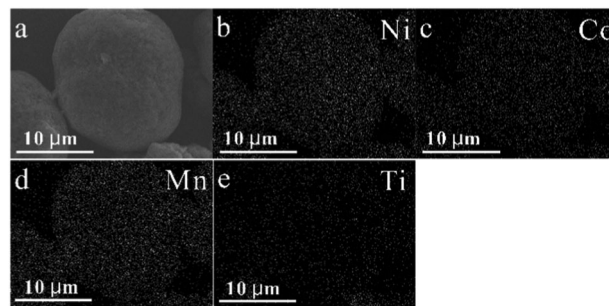


Fig. 2 SEM plot (a) and the corresponding EDS area maps of Ni (b), Co (c), Mn (d) and Ti (e) for 3%  $\text{TiO}_2@\text{NCMOH}$ .

NCM precursor. It is seen from Fig. 2 that the Ti (e) element distribution is completely overlapped with that of Ni (b), Mn (c) and Co (d) elements, indicating that  $\text{TiO}_2$  is coated on the NCM precursor surface uniformly.

The SEM images of morphologies and microstructures of the NCM, 1%  $\text{LTO}@\text{NCM}$ , 3%  $\text{LTO}@\text{NCM}$  and 5%  $\text{LTO}@\text{NCM}$  composite materials are shown in Fig. 3a–d, respectively, and the corresponding detailed views are shown as insets. Under high-magnification (Fig. 3a insets), it can be seen that the surfaces of NCM microspheres are smooth. The surface morphologies of  $\text{LTO}@\text{NCM}$  samples become fuzzy as the LTO coating content increases.

EDS area mapping analysis of 3%  $\text{LTO}@\text{NCM}$  composite material presented in Fig. 4 was performed to further identify the distribution of the LTO coating layer on the surface of coated NCM. It is seen from Fig. 4b–e that the Ti (e) element distribution is completely overlapped with that of Ni (b), Co (c) and Mn (d) elements, suggesting that LTO is clad on the LNMO surface uniformly.

To identify the interfacial structure of 3%  $\text{LTO}@\text{NCM}$  particles (which shows best electrochemical performances, shown later), we carried out TEM and surface EDS analyses, as seen in Fig. 5. Fig. 5a and b show high-resolution TEM (HRTEM) images of NCM and the 3%  $\text{LTO}@\text{NCM}$  particle, respectively. The surface

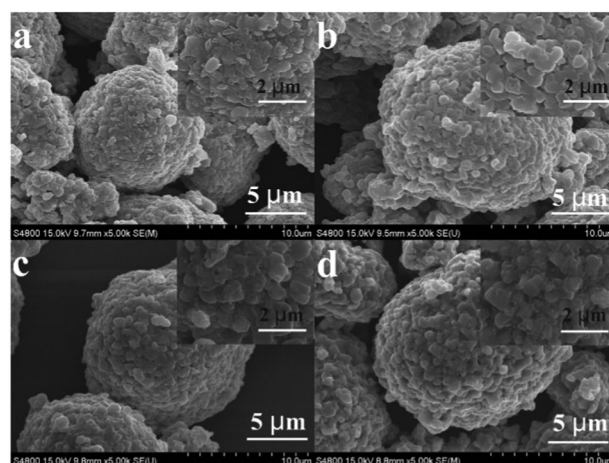


Fig. 3 SEM plots of (a) NCM, (b) 1%  $\text{LTO}@\text{NCM}$ , (c) 3%  $\text{LTO}@\text{NCM}$  and (d) 5%  $\text{LTO}@\text{NCM}$ . Insets are the corresponding detailed views.

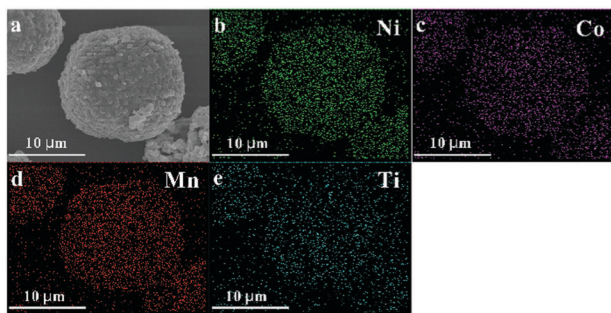


Fig. 4 SEM plot (a) and the corresponding EDS area maps of Ni (b), Co (c), Mn (d) and Ti (e) for 3% LTO@NCM.

of NCM is uniform without any coating layer as expected, while in 3% LTO@NCM an obvious coating layer appears with a thickness of *ca.* 14 nm. A small quantity of  $\text{Ni}^{2+}$ ,  $\text{Co}^{3+}$  and  $\text{Mn}^{4+}$

can be doped in  $\text{Li}_2\text{TiO}_3$  and a small amount of  $\text{Ti}^{4+}$  can be doped in the NCM structure during the calcination process. However, these migrating ions occupy a small amount of the total. A similar phenomenon was also observed in Li's results.<sup>28</sup> The high-resolution TEM (HRTEM) image of the 3% LTO@NCM particle shown in Fig. 5c presents a clear interplanar spacing lattice of 0.48 nm throughout the shell, which is in agreement with the *d*-spacing of the (002) crystal planes of the monoclinic  $\text{Li}_2\text{TiO}_3$ .<sup>30</sup> This means that the hierarchical LTO is coated successfully on the surface of NCM, as desired. The EDS elemental analysis results of selected areas marked as d and e regions in Fig. 5c are shown in Fig. 5d and e. The Ti atomic content of region d is four times higher than that of region e, suggesting that the surface layer is Ti-rich. The presence of Co, Mn and Ni elements is likely due to the doping of  $\text{Ni}^{2+}$ ,  $\text{Co}^{3+}$  and  $\text{Mn}^{4+}$  ions in  $\text{Li}_2\text{TiO}_3$ . This further suggests that the coating material is LTO.

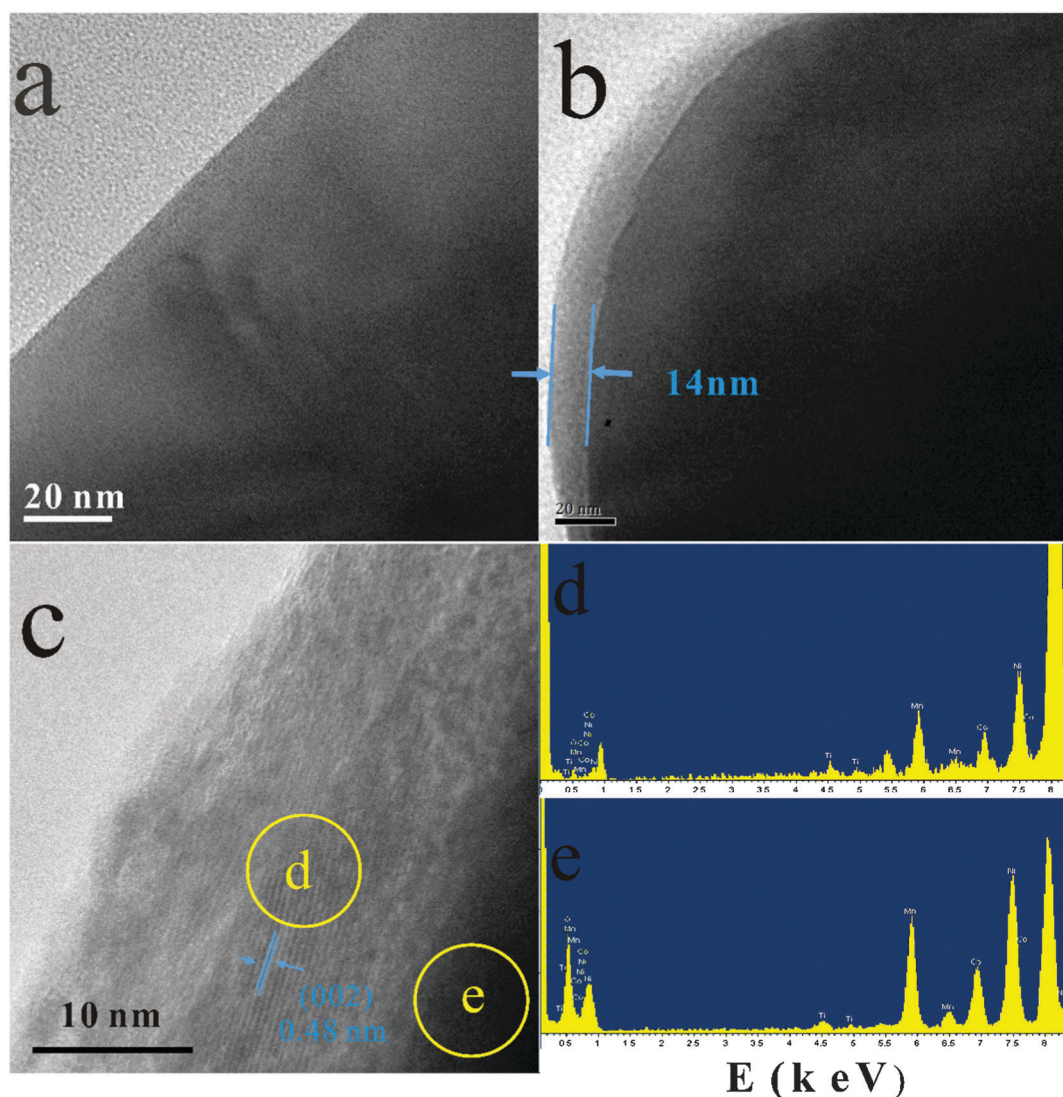


Fig. 5 (a) HR-TEM image of NCM, (b and c) HR-TEM image of 3% LTO@NCM, and (d and e) the corresponding surface EDS spectra of 3% LTO@NCM in the orange area in (c).

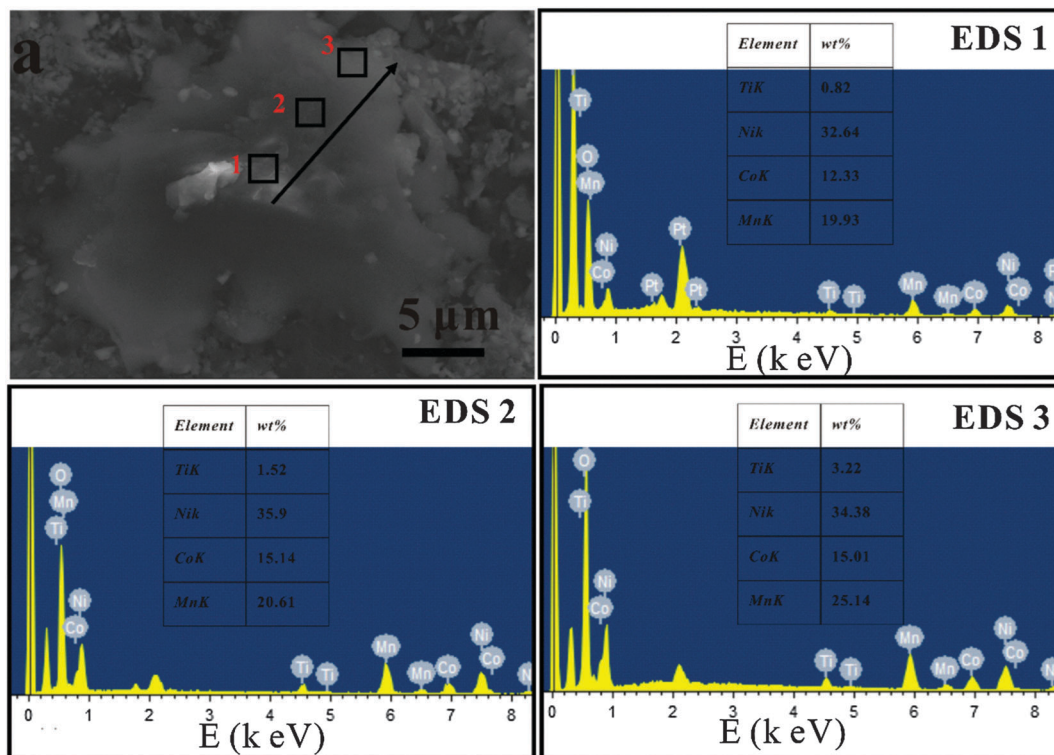


Fig. 6 SEM (a) and EDS (other three graphs) compositional change from the 3% LTO@NCM particle cross-section.

In order to further illustrate the Ti distribution, the cross-sectional SEM image of the 3% LTO@NCM particle and its corresponding EDS spectra were obtained, as shown in Fig. 6. The sample preparation was as follows. First, an adequate amount of 3% LTO@NCM powder was dispersed in a mixture solution of an epoxy resin and a solidifying agent. Second, the obtained mixture was put in a 60 °C oven for one day to solidify. Finally, the resultant solid was polished by metallographic sandpapers from rough to subtle to obtain the cross-section of 3% LTO@NCM. Three regions, from the core center to the outer layer (named regions 1–3, respectively), have been chosen to investigate the inner–external composition change of 3% LTO@NCM. It is noted that the weight ratio of Ni, Co and Mn is close to the stoichiometry and remains almost constant from regions 1 to 3, which indicates that the bulk of the material is  $\text{LiNi}_{0.5}\text{Co}_{0.2}\text{Mn}_{0.3}\text{O}_2$ . Besides, a slight amount of Ti is observed in the core center, and the content of Ti increases slowly from regions 1 to 3, which should be ascribed to the diffusion of some Ti during the calcination process. For region 3, the content of Ti is increased to 3.2%, more than the quadruple level of that in the core. Based on these EDS results, we speculate that most of the Ti ions accumulate on the outer layer of the particle to form LTO, while a partial amount of Ti ions enter the bulk  $\text{LiNi}_{0.5}\text{Co}_{0.2}\text{Mn}_{0.3}\text{O}_2$  with a gradient distribution. Thus, the Ti doped and LTO coated  $\text{LiNi}_{0.5}\text{Co}_{0.2}\text{Mn}_{0.3}\text{O}_2$  composite is confirmed.

The XRD patterns of the NCM and the LTO@NCM composite are shown in Fig. 7. All the samples exhibit a well-defined layer structure based on a hexagonal- $\text{NaFeO}_2$  structure with an

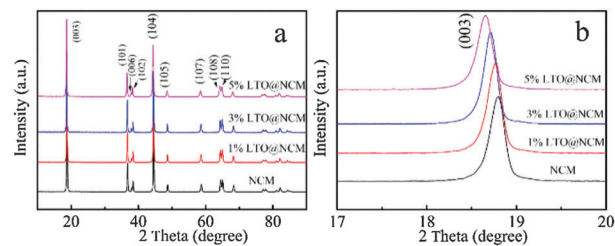


Fig. 7 (a) XRD plots of samples and (b) magnified graphs of (a) in a specific zone.

$R\bar{3}m$  space group and no impurities are present. However, a careful examination of the XRD patterns in a small region between 17 and 20° shows a slight shift to a lower angle along with an increase in the LTO coating content. The lattice parameters, the interlayer space of the (003) lattice plane, and the integrated intensity ratios of (003)/(104) obtained from the least square refinement based on a cubic structure using PDXL2 software (Rigaku, Japan) are summarized in Table 1. As seen from Table 1, both the crystal lattice parameter and the

Table 1 The summary of lattice parameters for all samples,  $d_{003}$ , and the integrated intensity ratios of (003)/(104) for the as-synthesized samples

Samples	<i>a</i> -Axis (Å)	<i>c</i> -Axis (Å)	<i>c/a</i>	<i>d</i> (003) (Å)	$I_{(003)}/I_{(104)}$
NCM	2.869	14.206	4.951	4.717	1.320
1%LTO@NCM	2.869	14.213	4.954	4.723	1.337
3%LTO@NCM	2.870	14.234	4.960	4.737	1.289
5%LTO@NCM	2.878	14.262	4.956	4.752	1.394

interlayer space of the (003) lattice plane of the samples increase as the LTO coating content increases, which is attributed to the substitution by some larger  $\text{Ti}^{4+}$  (0.605 Å) ions for smaller  $\text{Co}^{3+}$  (0.545 Å) ions and/or  $\text{Mn}^{4+}$  (0.53 Å) ions in the layered  $\text{LiNi}_{0.5}\text{Co}_{0.3}\text{Mn}_{0.2}\text{O}_2$  structure. The cation distribution in the lattice of the layered oxide is manifested by the intensity ratio  $I(003)/I(104)$ . If the intensity ratio  $I(003)/I(104)$  is lower than 1.2, a high degree of cation mixing is present, due to the occupancy of foreign ions in the lithium region.<sup>31–35</sup> It is noted that all the intensity ratios  $I(003)/I(104)$  are bigger than 1.2, indicating that low cation mixing occurred. ICP-AES was executed to identify the exact content of LTO in the composite material. The measured LTO values in 1% LTO@NCM, 3% LTO@NCM and 5% LTO@NCM are 0.87%, 2.82% and 4.8%, respectively, which are in good agreement with the designated values.

In order to observe the oxidation state of transition metals at the surface of 3% LTO@NCM, XPS test is performed, and the corresponding spectra are depicted in Fig. 8. All of the binding energies are revised using the C 1s peak (set to 284.6 eV) as the reference.

The binding energies of Ni 2p<sub>3/2</sub>/Ni 2p<sub>1/2</sub>, Co 2p<sub>3/2</sub>/Co 2p<sub>1/2</sub> and Mn 2p<sub>3/2</sub>/Mn 2p<sub>1/2</sub> on the surface of 3% LTO@NCM material are 854.3 eV/871.9 eV, 780.2 eV/795.4 eV and 642.5 eV/653.8 eV, which are consistent with the metal ion valences of Ni<sup>2+</sup>, Co<sup>3+</sup>, and Mn<sup>4+</sup>, respectively. These results are consistent with previous XPS results of NCM,<sup>36</sup> further indicating that coating modifications do not change the basic structure of NCM. Meanwhile, the Ti 2p<sub>3/2</sub> and Ti 2p<sub>1/2</sub> peaks of 3% LTO@NCM shown in Fig. 8d are located at 457.8 eV and 463.3 eV, in accordance with the Ti<sup>4+</sup> oxidation state of the Li<sub>2</sub>TiO<sub>3</sub> material.<sup>30</sup> This further indirectly proves that the surface coating material of LTO@NCM is Li<sub>2</sub>TiO<sub>3</sub>.

The electrochemical behaviors of the samples without and with LTO coating were investigated by CV tests, conducted at a scanning rate of 0.1 mV s<sup>-1</sup> at 25 °C, and depicted in Fig. 9. The intense and sharp reduction/oxidation peaks of Ni<sup>2+</sup>/Ni<sup>4+</sup> are

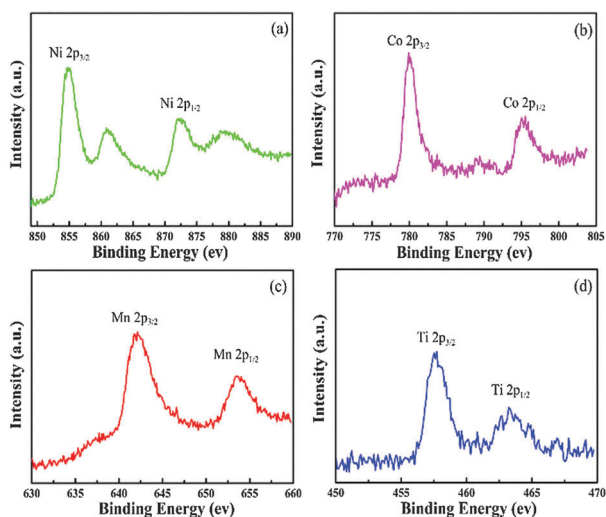


Fig. 8 XPS profiles of (a) Ni, (b) Co, (c) Mn, and (d) Ti on the surface of the 3% LTO@NCM composite material.

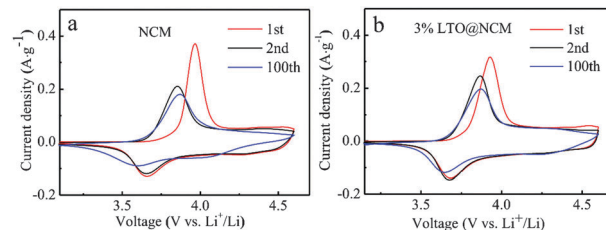


Fig. 9 CV plots at 25 °C with a scanning speed of 0.1 mV s<sup>-1</sup>: (a) NCM and (b) 3% LTO@NCM.

observed at around 3.8 V in both NCM and 3% LTO@NCM samples. After the first cycle, the oxidation peak of NCM shifts from 3.97 V to 3.86 V, while that of 3% LTO@NCM from 3.93 V to 3.87 V. The smaller difference in the oxidation peak position of 3% LTO@NCM between the first and second cycles means less polarization because LTO suppresses the side reaction between the electrolyte and NCM. The oxidation and reduction peaks of 3% LTO@NCM are sharper and the shift of the corresponding peaks between the first and second cycles is smaller compared with that of NCM, meaning that 3% LTO@NCM has better electrochemical reversibility and faster lithium insertion/extraction.<sup>37</sup> The reduction peak of NCM at the 100th cycle shifts to a lower potential than that of 3% LTO@NCM due to further polarization in NCM.

The initial discharge curves of the samples NCM, 1% LTO@NCM, 3% LTO@NCM and 5% LTO@NCM are plotted in Fig. 10 over the voltage range of 3–4.6 V at 0.2 C (34 mA g<sup>-1</sup>) at room temperature. After LTO coating, the plateaus corresponding to Li<sup>+</sup> ion extraction/insertion from/into the 3a sites do not change obviously, again indicating that LTO-coating does not change the basic structure of NCM (consistent with XRD results). The discharge capacities of NCM, 1% LTO@NCM, 3% LTO@NCM and 5% LTO@NCM are 187.8 mA h g<sup>-1</sup>, 186.2 mA h g<sup>-1</sup>, 182.2 mA h g<sup>-1</sup> and 179.2 mA h g<sup>-1</sup>, respectively. The small decline in discharge capacities along with the increase of the coating content is attributed to the calculated mass based on the composite material mass (Li<sub>2</sub>TiO<sub>3</sub> and LiNi<sub>0.5</sub>Co<sub>0.2</sub>Mn<sub>0.3</sub>O<sub>2</sub>) in the electrodes.

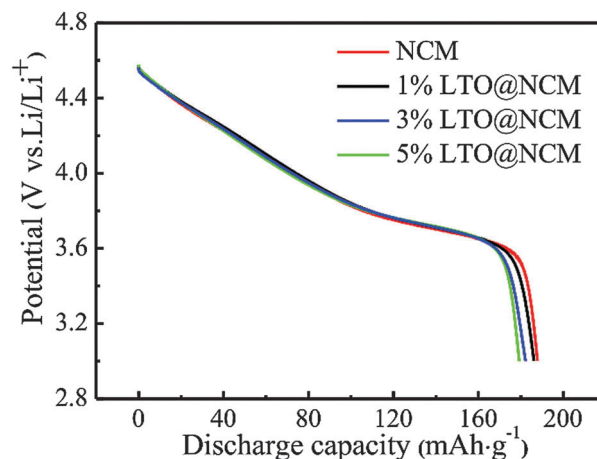


Fig. 10 First discharge profiles of samples at 0.2 C.

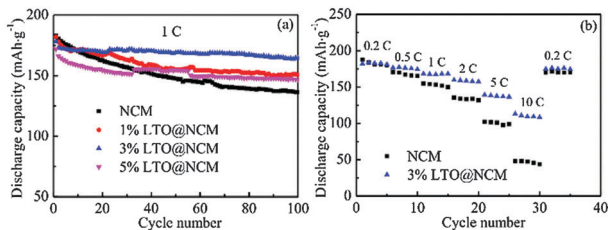


Fig. 11 Electrochemical properties of the as-prepared samples: (a) cycle performance at 1 C and (b) rate cycling performance of the samples.

The subsequent discharge cycle profiles at 1 C charge rate and 1 C discharge rate of the samples NCM, 1% LTO@NCM, 3% LTO@NCM and 5% LTO@NCM are shown in Fig. 11. Their first discharge capacities are 182.8, 181.8, 178.0 and 172.0  $\text{mA h g}^{-1}$ , respectively. After 100 cycles, the discharge capacities decrease steadily to 136.4, 150.6, 164.5 and 147.0  $\text{mA h g}^{-1}$ , which are equal to 74.3%, 82.8%, 92.4% and 85.4% of their first capacities, respectively. The capacity retention of 3% LTO@NCM is the highest, while that of 5% LTO@NCM is relatively low. This may be ascribed to the poor electric conductivity of LTO. So, an appropriate coating is beneficial, and the thicker coating layer increases the resistance for electron transportation among particles that is responsible for the lower discharge capacity of 5% LTO@NCM. Fig. 11(b) shows the rate performance of the NCM and the 3% LTO@NCM cathode material ranging from 0.2 C to 10 C. The discharge capacities of NCM at 0.2 C, 0.5 C, 1 C, 2 C, 5 C and 10 C are 180.0  $\text{mA h g}^{-1}$ , 165.5  $\text{mA h g}^{-1}$ , 149.9  $\text{mA h g}^{-1}$ , 131.7  $\text{mA h g}^{-1}$ , 99.2  $\text{mA h g}^{-1}$  and 43.8  $\text{mA h g}^{-1}$ , respectively. When the current value returned back to 0.2 C, a reversible discharge capacity of 170.4  $\text{mA h g}^{-1}$  is obtained, which is 90.7% of the initial discharge capacity at the same rate. After coating of 3% LTO, the specific discharge capacities are 180.1, 174.6, 168.4, 157.4, 136.5 and 108.2  $\text{mA h g}^{-1}$  at the rates of 0.2, 0.5, 1, 2, 5 and 10 C, respectively. As the current value is back to 0.2 C, the discharge capacity returns to 174.4  $\text{mA h g}^{-1}$ , which is 96.8% capacity retention of the initial discharge capacity at 0.2 C. The capacity of 3% LTO@NCM at 10 C is even higher than that of NCM at 5 C. Thus LTO coating facilitates Li ion transportation and stabilizes the NCM structure.

Electrochemical impedance spectroscopy was carried out to further illustrate the difference between NCM and 3% LTO@NCM regarding electrochemical polarization and ohmic polarization, as shown in Fig. 12. All the cells were charged at 1 C by the constant current and constant potential processes, and discharged *via* a constant current process for 20 and 60 cycles, and then the cathode was charged to 4.6 V. The EIS tests were performed in the range from 100 kHz to 0.005 Hz. The Nyquist plots of both materials display similar profiles with two semicircles in the high-frequency region, and their equivalent circuits are the same as shown in Fig. 12 insets. In the equivalent circuit,  $R_1$  is ascribed to electrolyte resistance, while  $R_2$  is attributed to the cathode surface film (similar to anode SEI layer) and direct charge transfer resistance of electrode materials and  $R_3$  is assigned to resistance of the anode. CPEs present the double layer capacitance or passivation film capacitance.

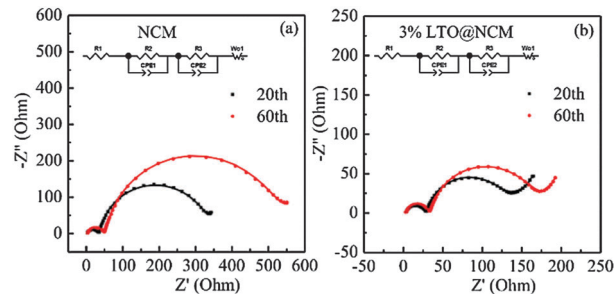


Fig. 12 EIS spectra of the samples in the frequency range between 0.005 Hz and 100 kHz at 25 °C. The insets show the equivalent circuits for the EIS measurements.

Wo represents the Warburg impedance.<sup>38,39</sup> The solid line is the fitted results of measured data (dotted value). It is clearly seen that the equivalent circuit model is adequate for the fitting as the dotted and solid lines are overlapping. The fitted values of these components are listed in Table 2. Obviously, the LTO-coating NCM electrode exhibits a much smaller charge-transfer resistance than that of the pristine NCM electrode, indicating that LTO modification of the NCM material is favourable for lithium ion mobility. The  $R_2$  values of 3% LTO@NCM at the 20th cycle is 24.8, while that of NCM is 30.4  $\Omega$ . The  $R_2$  and  $R_3$  values of 3% LTO@NCM cathode at the 60th cycle do not change much compared with those at the 20th cycle. However, the  $R_2$  and  $R_3$  values of the NCM cathode at the 60th cycle increased by half compared with those at the 20th cycle. According to previous literature reports,  $\text{Ni}^{4+}$  ions formed at the deintercalation state of the cathode ( $\text{Li}_{1-x}\text{Ni}_{0.5}\text{Co}_{0.2}\text{Mn}_{0.3}\text{O}_2$ ) are reactive toward liquid electrolyte and can catalyze the oxidation of the electrolyte, triggering the oxygen loss from the surface of the material, accompanied by a phase transformation from the rhombohedral phase to a mix of spinel and rock salt phases, which is the major reason for the capacity fading of NCM during the cycle performance.<sup>15</sup> Based upon the better cycling performance presented in this work, it is obvious that the LTO can serve as a protective layer to inhibit the electrolyte decomposition at the electrode/electrolyte interface and thereby lower the interface charge transfer resistance, and improve the structural integrity and its capacity retention during long-term charge-discharge cycles.

CV scanning was performed to further explain the different electrochemical behaviors of the samples. The cells were charged and discharged at the rate of C/20 for one cycle prior to the CV scanning. Fig. 13 shows the CV plots of NCM and 3% LTO@NCM samples at various scan rates from 0.2 to 1  $\text{mV s}^{-1}$ . As seen in Fig. 13, the peak current density is proportional to the square root of the scanning rate, indicating that the

Table 2 Impedance parameter of electrodes

	$R_1(\Omega)$	$R_2(\Omega)$	$R_3(\Omega)$
NCM (20th)	2.1	30.4	272.0
NCM (60th)	2.8	44.6	438.7
3% LTO@NCM (20th)	3.1	24.8	86.6
3% LTO@NCM (60th)	3.1	28.3	114.9

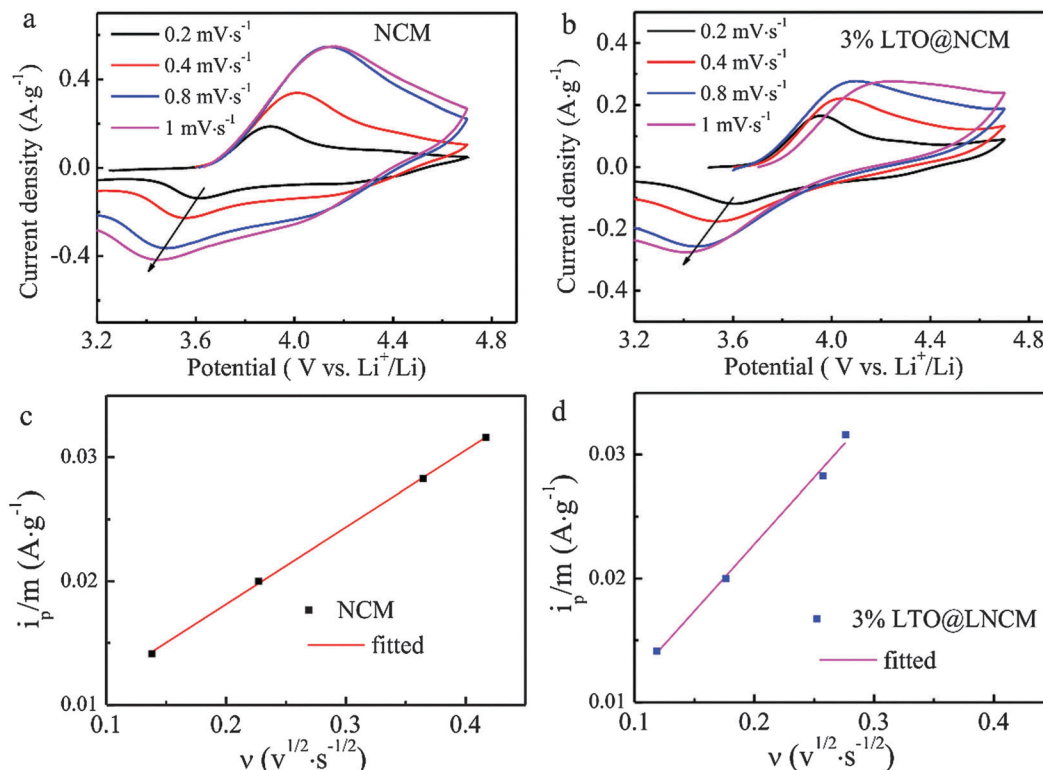


Fig. 13 CV plots of (a) NCM and (b) 3% LTO@NCM at different scan rates; and the plots of reductive peak current density (*i*<sub>p</sub>) as a function of the square root of the scan rate ( $\nu^{1/2}$ ) for (c) NCM and (d) 3% LTO@NCM.

electrode reaction is a reversible process. For a reversible reaction, the peak current density during oxidative–reductive scans at different rates can be used to calculate the Li<sup>+</sup> diffusion coefficient ( $D_{\text{Li}}$ ) using the Randles–Sevcik equation:<sup>40</sup>

$$i_p/m = 0.4463 n^{3/2} F^{3/2} C_{\text{Li}} A_e R^{-1/2} T^{-1/2} D_{\text{Li}}^{1/2} \nu^{1/2} \quad (1)$$

where  $n$ ,  $F$ ,  $C_{\text{Li}}$ ,  $A_e$ ,  $R$ ,  $T$ , and  $\nu$  are the number of electrons per molecule during the redox process, Faraday's constant, the concentration of lithium ions, the surface area, the gas constant, the absolute temperature and the scanning rate, respectively. Fig. 13c and d present the  $i_p/m - \nu^{1/2}$  plots, the relationship between  $i_p/m$  and  $\nu^{1/2}$  is linear. According to eqn (1), the Li<sup>+</sup> coefficients of NMO and 3% LTO@NCM are calculated to be approximately  $5.57 \times 10^{-11}$  and  $1.68 \times 10^{-10}$  cm<sup>2</sup> s<sup>-1</sup>, respectively. Clearly, the Li<sup>+</sup> diffusion coefficient is found to be greatly improved due to the LTO coating.

Fig. 14 shows the cycle performance of NCM and 3% LTO@NCM electrodes at 55 °C at 1 C rate. The NCM and 3% LTO@NCM materials exhibit specific discharge capacities of 198.0 and 197.3 mA h g<sup>-1</sup> at the first cycle, respectively. The obvious difference is that the capacity of NCM faded quickly, with a capacity retention of 63.9% after 100 cycles, whereas the capacity of 3% LTO@NCM faded gradually and was 83.7% of the initial capacity after 100 cycles. From these results, we believe that the LTO coating layer can form a stable barrier between NCM and the electrolyte at elevated temperatures to prevent the side reactions between them and thereby enhance the electrode performance at high-temperatures.

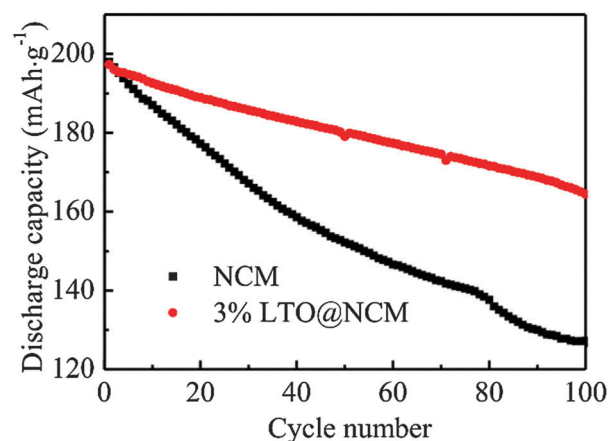


Fig. 14 Cycle performance of NCM and 3% LTO@NCM at 1 C at 55 °C.

Table 3 presents the concentrations of Ni, Co and Mn cations of NCM and 3% LTO@NMO dissolved in the electrolyte. The cell was charged to a fully delithiated state at 0.2 C, then unpacked to obtain the electrode material film in an Ar-filled

Table 3 The concentration of Ni, Co and Mn cations dissolved in the electrolyte for NCM and 3% LTO@NCM electrodes stored at 80 °C for 12 h

	Ni (ppm)	Co (ppm)	Mn (ppm)
NCM	7.08	2.58	6.06
3% LTO@NCM	5.67	2.20	4.50

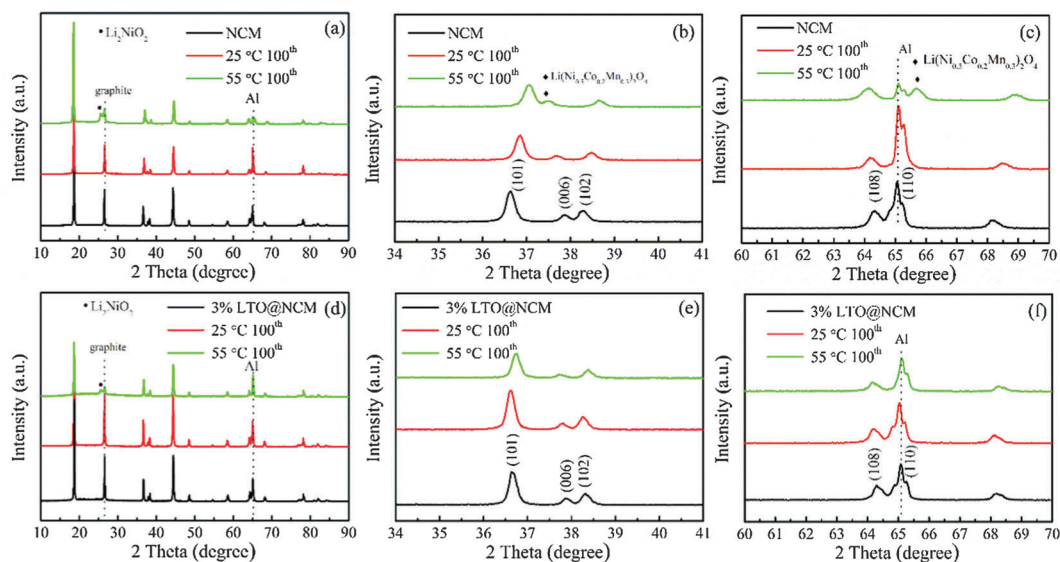


Fig. 15 *Ex situ* XRD patterns of NCM (a–c) and 3% LTO@NCM (d–f): before cycle (black line), after the 100th cycle at 25 °C (red line) and after the 100th cycle at 55 °C (green line).

glove box. The electrode film was immersed in 301 electrolyte with the ratio of electrode materials to electrolyte being 2 mg to 1 ml at 80 °C for 12 h. After acid-treatment to remove organic materials, the storage electrolyte was subjected to metal ion test using an ICP instrument. The concentrations of Ni and Co, especially of Mn cations of 3% LTO@NCM dissolved in the electrolyte are lower than those of NCM, which suggests that the LTO coating layer successfully alleviated the dissolution of transition metals and stabilized the NCM structure. This LTO protective coating suppressed the HF scavenging of NCM in electrolyte, leading to enhanced electrochemical properties.

To examine the structural stability of NCM and 3% LTO@NCM, *ex situ* XRD studies of electrodes were performed before and after charge–discharge processes at 25 °C and 55 °C, as shown in Fig. 15 (black lines are electrodes before cycle, red lines are after the 100th cycle at 25 °C and green lines are after the 100th cycle at 55 °C). The samples were cycled for 100 cycles at 1 C before the XRD measurements. When cycled at 25 °C, the structures of NCM and 3% LTO@NCM do not change much, and peak positions did not change. However, when cycled at 55 °C, the (006) peak of NCM shifted toward smaller  $2\theta$  moving close to the (101) peak and a new peak emerged at around 65.7°, which are all attributed to the Li deficient spinel  $\text{Li}(\text{Ni}_{0.5}\text{Co}_{0.2}\text{Mn}_{0.3})_2\text{O}_4$  phase. On the other hand, in the case of 3% LTO@NCM, the (006) peak does not change and the new peak is absent, implying the more stable structure of NCM after LTO-coating. The new peak at around 25.7° that appeared in both NCM and 3% LTO@NCM when cycled at 55 °C may be ascribed to the  $\text{Li}_2\text{NiO}_2$  phase. At room temperature, the spinel phase transformation and the side reaction of the layered structure are not obvious, so the XRD patterns recorded before and after cycles are the same.<sup>15</sup> While at high temperatures, the oxygen evolution in Ni-based layered structures is severe accompanied by a structural transformation from layered  $\text{LiMO}_2$  into a spinel structure.<sup>11</sup>

Nevertheless, LTO coating successfully suppresses the oxygen loss from the surface of the material, consequently the structure of NCM becomes more stable. This is also the reason that the electrochemical properties and the rate capacity of 3% LTO@NCM are superior to those of pristine NCM.

The thermal behaviors of charged (delithiated, 4.6 V) NCM and 3% LTO@NCM in 301 electrolyte (1M LiPF<sub>6</sub>, EC/DMC) were investigated by DSC/TG analysis as shown in Fig. 16. The onset exothermic temperatures for these two samples are both at *ca.* 181.2 °C, however the total heat quantity for 3% LTO@NCM around 180–350 °C is 1478 J g<sup>-1</sup>, while that of NCM is 1764 J g<sup>-1</sup>. The third exothermic peak of NCM shifted from 287.3 °C to 305.3 °C after 3% LTO coating. LTO working as a protective layer observably inhibits the interaction between NCM and the electrolyte, and suppresses the electrolyte

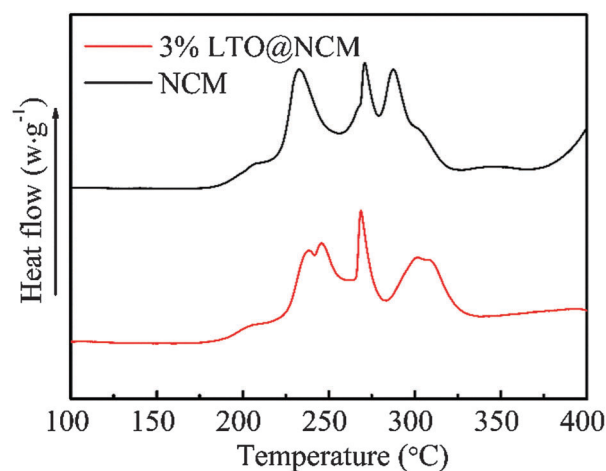


Fig. 16 DSC curves of samples in #301 electrolyte at the states of charged to 4.6 V.

decomposition at the electrode/electrolyte interface, thereby improving the thermostability of NCM.

## Conclusions

In summary, we developed a simple and commercially feasible method to modify the NCM surface with LTO coating. Structural characterization by SEM, XRD and TEM show that the coating is uniform, and the structure of NCM is retained. The electrochemical tests demonstrate that LTO coating improves the electrochemical performance of NCM. The coating content of LTO up to 3% in the NCM exhibits excellent electrochemical cycle, presenting a discharge specific capacity of 178.0 mA h g<sup>-1</sup> at 1 C with a retention of 92.4% after 100 cycles. In addition, it also shows remarkable rate capability, the discharge specific capacity decreased slightly from 180.1 to 174.6, 168.4, 157.4, 136.5 and 108.2 mA h g<sup>-1</sup> at 0.2 C, 0.5 C, 1 C, 2 C, 5 C and 10 C, respectively. Furthermore, it has superior electrochemical properties at elevated temperatures and high rates. At 1 C rate at 55 °C, the discharge capacity of 3% LTO@NCM is up to 197.3 mA h g<sup>-1</sup>, with a retention of 83.4% after 100 cycles. Also, the phase transformation of NCM at high-temperatures and that of metal ions are effectively suppressed after LTO-coating. These results illustrate that LTO coating can work as an isolating layer to inhibit the interaction between the NCM cathode and the electrolyte, alleviate the dissolution of metal ions and phase transformation in NCM, and improve its structural stability.

## Acknowledgements

The authors gratefully acknowledge the financial support from the National High Technology Research and Development Program of China (2012AA110204), Key Project of Science and Technology of Fujian Province (2013H6022), Science and Technology Bureau of Xiamen (Grant No. 3502Z20133004), National Natural Science Foundation of China (21321062) and National Found for Fostering Talents of Basic Science (J1310024). The authors also wish to express their thanks to Drs Dong Sun and Binbin Xu for their valuable suggestions.

## Notes and references

- X. Liu, Y. J. Wang, B. Barbiellini, H. Hafiz, S. Basak, J. Liu, T. Richardson, G. Shu, F. Chou, T.-C. Weng, D. Nordlund, D. Sokaras, B. Moritz, T. P. Devereaux, R. Qiao, Y.-D. Chuang, A. Bansil, Z. Hussain and W. Yang, *Phys. Chem. Chem. Phys.*, 2015, **17**, 26369–26377.
- X. Feng, Z. Z. Yang, D. C. Tang, Q. Y. Kong, L. Gu, Z. X. Wang and L. Q. Chen, *Phys. Chem. Chem. Phys.*, 2015, **17**, 1257–1264.
- J. Wang, W. Lin, B. Wu and J. Zhao, *J. Mater. Chem. A*, 2014, **2**, 16434–16442.
- J. Wang, Y. Yu, B. Wu, W. Lin, J. Li and J. Zhao, *J. Mater. Chem. A*, 2015, **3**, 2353–2360.
- B. Li, Y. Yu and J. Zhao, *J. Power Sources*, 2015, **275**, 64–72.
- J. B. Goodenough and K.-S. Park, *J. Am. Chem. Soc.*, 2013, **135**, 1167–1176.
- T. Ohzuku and R. J. Brodd, *J. Power Sources*, 2007, **174**, 449–456.
- O. K. Park, Y. Cho, S. Lee, H. C. Yoo, H. K. Song and J. Cho, *Energy Environ. Sci.*, 2011, **4**, 1621–1633.
- B. Scrosati and J. Garche, *J. Power Sources*, 2010, **195**, 2419–2430.
- X. Xiong, Z. Wang, H. Guo, Q. Zhang and X. Li, *J. Mater. Chem. A*, 2013, **1**, 1284–1288.
- M. Jo, M. Noh, P. Oh, Y. Kim and J. Cho, *Adv. Energy Mater.*, 2014, **4**, 1301583.
- M. Zou, M. Yoshio, S. Gopukumar and J.-I. Yamaki, *Chem. Mater.*, 2003, **15**, 4699–4702.
- Y. Kim, *Phys. Chem. Chem. Phys.*, 2013, **15**, 6400–6405.
- X. Yang, X. Wang, L. Hu, G. Zou, S. Su, Y. Bai, H. Shu, Q. Wei, B. Hu, L. Ge, D. Wang and L. Liu, *J. Power Sources*, 2013, **242**, 589–596.
- S.-K. Jung, H. Gwon, J. Hong, K.-Y. Park, D.-H. Seo, H. Kim, J. Hyun, W. Yang and K. Kang, *Adv. Energy Mater.*, 2014, **4**, 1300787.
- Y.-K. Sun, B.-R. Lee, H.-J. Noh, H. Wu, S.-T. Myung and K. Amine, *J. Mater. Chem.*, 2011, **21**, 10108–10112.
- D.-J. Lee, B. Scrosati and Y.-K. Sun, *J. Power Sources*, 2011, **196**, 7742–7746.
- D. W. Shin, C. A. Bridges, A. Huq, M. P. Paranthaman and A. Manthiram, *Chem. Mater.*, 2012, **24**, 3720–3731.
- Y.-K. Sun, S.-T. Myung, M.-H. Kim, J. Prakash and K. Amine, *J. Am. Chem. Soc.*, 2005, **127**, 13411–13418.
- L. Li, Z. Chen, Q. Zhang, M. Xu, X. Zhou, H. Zhu and K. Zhang, *J. Mater. Chem. A*, 2015, **3**, 894–904.
- L. Li, Z. Chen, L. Song, M. Xu, H. Zhu, L. Gong and K. Zhang, *J. Alloys Compd.*, 2015, **638**, 77–82.
- J. Zhang, Z. Li, R. Gao, Z. Hu and X. Liu, *J. Phys. Chem. C*, 2015, **119**, 20350–20356.
- S. B. Jang, S. H. Kang, K. Amine, Y. C. Bae and Y. K. Sun, *Electrochim. Acta*, 2005, **50**, 4168–4173.
- H. B. Kim, B. C. Park, S. T. Myung, K. Amine, J. Prakash and Y. K. Sun, *J. Power Sources*, 2008, **179**, 347–350.
- W. Liu, M. Wang, X. L. Gao, W. Zhang, J. Chen, H. Zhou and X. Zhang, *J. Alloys Compd.*, 2012, **543**, 181–188.
- J. Liu and A. Manthiram, *Chem. Mater.*, 2009, **21**, 1695–1707.
- Y. Bai, X. Wang, S. Yang, X. Zhang, X. Yang, H. Shu and Q. Wu, *J. Alloys Compd.*, 2012, **541**, 125–131.
- J. Lu, Q. Peng, W. Wang, C. Nan, L. Li and Y. Li, *J. Am. Chem. Soc.*, 2013, **135**, 1649–1652.
- H. Deng, P. Nie, H. Luo, Y. Zhang, J. Wang and X. Zhang, *J. Mater. Chem. A*, 2014, **2**, 18256–18262.
- X. Yang, R. Yu, L. Ge, D. Wang, Q. Zhao, X. Wang, Y. Bai, H. Yuan and H. Shu, *J. Mater. Chem. A*, 2014, **2**, 8362.
- J. Li, R. Yao and C. Cao, *ACS Appl. Mater. Interfaces*, 2014, **6**, 5075–5082.
- C. Nithya, R. Thirunakaran, A. Sivashanmugam and S. Gopukumar, *ACS Appl. Mater. Interfaces*, 2012, **4**, 4040–4046.

- 33 M. Wang, Y. Chen, F. Wu, Y. Su, L. Chen and D. Wang, *Electrochim. Acta*, 2010, **55**, 8815–8820.
- 34 Y.-M. Choi, S.-I. Pyun and S.-I. Moon, *Solid State Ionics*, 1996, **89**, 43–52.
- 35 L. Liang, K. Du, Z. Peng, Y. Cao, J. Duan, J. Jiang and G. Hu, *Electrochim. Acta*, 2014, **130**, 82–89.
- 36 Y.-M. Lee, K.-M. Nam, E.-H. Hwang, Y.-G. Kwon, D.-H. Kang, S.-S. Kim and S.-W. Song, *J. Phys. Chem. C*, 2014, **118**, 10631–10639.
- 37 Y. Zhu and C. Wang, *J. Phys. Chem. C*, 2010, **115**, 823–832.
- 38 L. J. Xi, H.-E. Wang, Z. G. Lu, S. L. Yang, R. G. Ma, J. Q. Deng and C. Y. Chung, *J. Power Sources*, 2012, **198**, 251–257.
- 39 S. J. Shi, J. P. Tu, Y. Y. Tang, X. Y. Liu, Y. Q. Zhang, X. L. Wang and C. D. Gu, *Electrochim. Acta*, 2013, **88**, 671–679.
- 40 H. Guo, C. Wu, J. Xie, S. Zhang, G. Cao and X. Zhao, *J. Mater. Chem. A*, 2014, **2**, 10581–10588.